Exact Stability Boundaries and Chenciner Bifurcation in a Car-Following Map with State Dependent Delayed Response

HAFIDH KHOERUL FATA*, ROBERTUS HERI SOELISTYO UTOMO,
YUSEPHUS DECUPERTINO SUMANTO
Department of Mathematics, Faculty of Science and Mathematics
Diponegoro University
Semarang 50275,
INDONESIA

Corresponding Author

Abstract: At uniform following, reaction delay is characterized by its value and headway sensitivity. We derive a three-dimensional car-following map that separates these quantities. The Jury conditions yield the Schur stability region and a closed-form Neimark–Sacker boundary. Headway sensitivity is absent from the Jacobian but enters the nonlinear terms, making the first Lyapunov coefficient quadratic in this sensitivity within the local function class. For a hyperbolic-tangent benchmark, criticality changes while the linear boundary remains fixed, and a fifth-order normal form identifies a Chenciner point numerically. Continuation locates the associated invariant-curve fold and assesses the local predictor. Basin and time-response computations demonstrate coexistence of stable uniform following and an oscillatory attractor. These results concern one leader–follower pair; disturbance propagation along a platoon requires a multi-vehicle model.

Keywords: car-following map; state-dependent delay; Schur stability; Neimark–Sacker bifurcation; Chenciner bifurcation; invariant-curve fold; bistability.

Received: June 11, 2026. Revised: July 24, 2026. Accepted: August 16, 2026. Published: November 10, 2026.

1 Introduction

Stop-and-go waves can arise without physical road bottlenecks. Ring-road experiments have shown that small perturbations of an initially homogeneous flow can amplify into traffic jams that propagate against the direction of travel, [1]. In a car-following model, the simplest reference state is motion with constant speed and constant inter-vehicle headway, which is referred to as the uniform-following equilibrium. The optimal-velocity model relates vehicle acceleration to the desired speed determined by the headway, [2], whereas the full velocity-difference model (FVDM) also accounts for the relative speed with respect to the preceding vehicle, [3]. Within the class of optimal-velocity models, parameter changes can destabilize the uniform-following equilibrium through a Hopf bifurcation, followed by the emergence of periodic solutions, [4].

An optimal-velocity model with explicit delay showed that sufficiently large delays can generate distinct congestion patterns, [5]. Periodic solutions were subsequently analyzed in a car-following model with a reaction time delay, [6]. The Hopf bifurcation was further shown to be robustly subcritical, allowing a stable uniform-following equilibrium to coexist with stop-and-go waves, [7]. In the subcritical Hopf regime reported in [7], small perturbations decay to equilibrium, whereas larger perturbations develop into stop-and-go oscillations.

The reaction time may also depend on the vehicle state. Driver memory was represented through a state-dependent delay, with analysis of the resulting stability region and hysteresis, [8]. A model with a headway-dependent reaction time exhibited a bistable region in which smooth traffic and stop-and-go traffic occur at the same parameter values, depending on the magnitude of the initial perturbation, [9].

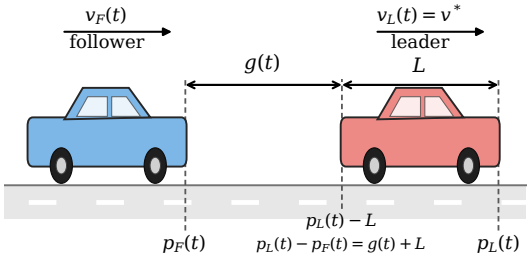
In a discrete-time setting, a continuous car-following model was discretized into a difference equation, with stability conditions derived using discrete control theory, [10]. A delayed coupled-map car-following model was also studied, with feedback control constructed within a linear discrete-time systems framework, [11].

Models incorporating driver-reaction and mechanical delays have also been analyzed for stability changes, oscillatory solutions, and Hopf bifurcation, [12].

Table 1 (Appendix) compares the delay formulations and types of analyses used in the cited studies. The map developed here separates the delay value at equilibrium from its local sensitivity to the headway. The objective is to determine whether a change in delay sensitivity can alter bifurcation criticality without shifting the linear stability boundary.

A reaction delay shorter than one update interval is represented as a combination of the current response and the response one step earlier. In the linearization, the delayed-response weight at the uniform-following equilibrium enters the Jacobian and determines the linear stability boundary, whereas the local delay sensitivity is absent from the characteristic polynomial.

The local delay sensitivity first enters the quadratic terms of the map. At the Neimark–Sacker boundary, Proposition 4.1 shows that the first Lyapunov coefficient is quadratic in this sensitivity. Hence, the linear boundary can remain fixed while the bifurcation



Source: created by the authors.

Figure 1: The diagram places $p_F(t)$ and $p_L(t)$ at the front bumpers of the follower and leader. The leader rear bumper is at $p_L(t) - L$, so $g(t) = [p_L(t) - L] - p_F(t)$; the arrow labeled L spans the leader length.

changes from supercritical to subcritical. At $\ell_1 = 0$, the cubic radial term vanishes; therefore, Section 4.2 continues the normal form to fifth order and derives the local invariant-curve fold predictor.

The criticality change and fold location near the Chenciner point were tested numerically. Numerical continuation is compared with the normal-form prediction, while a basin section is used to examine the coexistence of the uniform-following equilibrium and an oscillatory response at the same parameter values. Single-pair reduction does not address disturbance propagation along a multi-vehicle chain.

2 Model Formulation

Consider a follower vehicle moving behind the leader, as shown in Figure 1. To fix the coordinate convention, a reference point was placed at the front bumper of each vehicle. Let $p_L(t)$ and $p_F(t)$ denote the longitudinal positions of the leader and follower front bumpers, respectively, and let $L > 0$ be the effective vehicle length subtracted from the front-to-front distance. The net headway is

$$g(t) = p_L(t) - p_F(t) - L, \tag{1}$$

with $v_L(t) = \dot{p}_L(t)$ and $v_F(t) = \dot{p}_F(t)$, so that

$$\dot{g}(t) = v_L(t) - v_F(t). \tag{2}$$

At the uniform-following equilibrium, the headway and both vehicle speeds are constant,

$$\begin{aligned} g(t) &\equiv g^*, \\ v_L(t) = v_F(t) &\equiv v^*, \qquad v^* = V(g^*). \end{aligned} \tag{3}$$

where g^* and v^* denote the equilibrium headway and speed, respectively. The function V maps the headway to the desired speed.

The leader is assumed to travel at a constant speed, $v_L(t) \equiv v^*$. The follower acceleration obeys an FVDM-type law,

$$\begin{aligned} \dot{v}_F(t) = \gamma_v \left[V(g(t - \tau_{\text{phys}}(g(t)))) - v_F(t)\right] \\ + \gamma_\Delta \left[v^* - v_F(t)\right], \end{aligned} \tag{4}$$

where $\gamma_v > 0$ and $\gamma_\Delta \geq 0$ are fixed response coefficients. The second term retains the relative speed correction of the FVDM, [3]. The function $\tau_{\text{phys}}(g)$ is a headway-dependent reaction time, as in the headway-dependent delay formulations of car-following dynamics, [9]. The delay affects the optimal velocity response, whereas the relative speed correction uses the current state.

Let $S > 0$ be a length scale, $T > 0$ a time scale, and $U = S/T$. Deviations from the uniform-following equilibrium are written as

$$x = \frac{g - g^*}{S}, \qquad y = \frac{v^* - v_F}{U}. \tag{5}$$

The variables $x(t)$ and $y(t)$ in (5) measure the headway perturbation from g^* and the scaled relative speed, respectively. The change in optimal velocity induced by a headway perturbation is represented by

$$\psi(x) = \frac{V(g^* + Sx) - V(g^*)}{U}, \tag{6}$$

so that $\psi(0) = 0$.

Use dimensionless time $\theta = t/T$. Since $U = S/T$ and v^* is constant,

$$\frac{dx}{d\theta} = y, \qquad \frac{dy}{d\theta} = -\frac{T}{U}\dot{v}_F. \tag{7}$$

If g_τ and x_τ denote the headway and headway perturbation at the delayed time, respectively, then

$$V(g_\tau) - v_F = U\big[\psi(x_\tau) + y\big]. \tag{8}$$

Using (7)–(8), substitution of (5) and (6) into (4) gives

$$\frac{dx}{d\theta} = y, \qquad \frac{dy}{d\theta} = -\kappa_v y - \alpha\psi(x_\tau), \tag{9}$$

where

$$\kappa_v = T(\gamma_v + \gamma_\Delta), \qquad \alpha = T\gamma_v. \tag{10}$$

The vehicle response is updated at dimensionless times $\theta_n = nh$, with $h > 0$. The physical update interval is $\Delta t = hT$. For a reaction time contained within one update interval,

$$0 \leq \tau_{\text{phys}}(g^* + Sx) \leq hT. \tag{11}$$

At θ_n, the delay time lies between two consecutive update times. The delayed optimal-velocity response in (9) is represented by linear interpolation,

$$\begin{aligned} \psi(x_{\tau,n}) \approx [1 - \rho(x_n)]\psi(x_n) \\ + \rho(x_n)\psi(x_{n-1}), \end{aligned} \tag{12}$$

where

$$\rho(x) = \frac{\tau_{\text{phys}}(g^* + Sx)}{hT}, \qquad 0 \leq \rho(x) \leq 1. \tag{13}$$

In the interpolation (12), the weight ρ is defined by (13); $\rho = 0$ uses the response at the current update time, whereas $\rho = 1$ uses the response one update earlier. For $z = x_{n-1}$, define

$$\Phi(x, z) = [1 - \rho(x)]\psi(x) + \rho(x)\psi(z). \tag{14}$$

The interval hT represents the response update time. With

$$\mu = h\kappa_v, \qquad a = h\alpha, \qquad z_n = x_{n-1}, \tag{15}$$

a one-step discretization of (9) with the delayed response (14) gives

$$\begin{aligned} x_{n+1} &= x_n + hy_n, \\ y_{n+1} &= (1-\mu)y_n - a\Phi(x_n, z_n), \\ z_{n+1} &= x_n. \end{aligned} \tag{16}$$

If $X_n = (x_n, y_n, z_n)^\top$, then (16) defines the map $X_{n+1} = F(X_n)$ in a three-dimensional state space.

At a fixed point, $y = 0$ and $z = x$. Since $\Phi(x, x) = \psi(x)$, it follows that

$$\mathrm{Fix}(F) = \{(\xi, 0, \xi) : \psi(\xi) = 0\}. \tag{17}$$

If V is strictly increasing on the headway interval under consideration, then

$$\begin{aligned} \psi(\xi) = 0 &\iff V(g^* + S\xi) = V(g^*) \\ &\iff \xi = 0, \end{aligned} \tag{18}$$

hence $E_0 = (0, 0, 0)$ is the unique uniform-following equilibrium on the assumed headway interval.

The reaction-delay value at equilibrium and its local variation with headway are

$$\begin{aligned} r = \rho(0) &= \frac{\tau_{\mathrm{phys}}(g^*)}{hT}, \\ d = \rho'(0) &= \frac{S}{hT}\tau'_{\mathrm{phys}}(g^*). \end{aligned} \tag{19}$$

The coefficient r in (19) is the reaction time at the uniform-following equilibrium relative to one update interval, whereas d measures the local change in the delay fraction induced by a headway perturbation. In general, $0 \le r \le 1$ and $d \in \mathbb{R}$; Sections 3–5 use $0 < r < 1$.

3 Linear Stability and the Neimark–Sacker Boundary

The local stability of the uniform-following equilibrium E_0 is determined by the multipliers of the linearization of (16). After scaling, the sensitivity of the desired speed to headway changes near g^* is $s = \psi'(0) = TV'(g^*) > 0$. Define $q = has > 0$, which measures the effective strength of the follower's adjustment to headway changes over one update interval. For fixed h and s, varying q is equivalent to varying the gain a through $a = q/(hs)$. Section 3 assumes $0 < \mu < 2$ and $0 < r < 1$.

3.1 Schur Conditions and Stability Boundaries

To state the stability boundaries, define

$$\begin{aligned} q_{\mathrm{NS}} = &\frac{\sqrt{[1+(1-\mu)r]^2 + 4\mu r^2}}{2r^2} \\ &- \frac{1+(1-\mu)r}{2r^2}. \end{aligned} \tag{20}$$

Also set $q_D = 1/r$ and $\mu_c(r) = 1 + 1/(2r)$, and define $q_F = 2(2-\mu)/(2r-1)$ for $r > 1/2$.

Proposition 3.1. *For $0 < \mu < 2$, $0 < r < 1$, and $h, a, s > 0$, the equilibrium E_0 is Schur stable if and only if $0 < q < q_c$, where*

$$q_c = \begin{cases} q_{\mathrm{NS}}, & \mu < \mu_c(r), \\ q_D, & \mu = \mu_c(r), \\ q_F, & \mu > \mu_c(r). \end{cases} \tag{21}$$

Proof. Differentiating (14) with respect to x and z gives

$$\begin{aligned} \Phi_x(x, z) &= [1-\rho(x)]\psi'(x) \\ &\quad + \rho'(x)[\psi(z) - \psi(x)], \\ \Phi_z(x, z) &= \rho(x)\psi'(z). \end{aligned} \tag{22}$$

Evaluating at $(x, z) = (0, 0)$ with $\psi(0) = 0$, $\rho(0) = r$, and $\rho'(0) = d$ gives

$$\begin{aligned} \Phi_x(0,0) &= (1-r)s + d[\psi(0) - \psi(0)] \\ &= s(1-r), \\ \Phi_z(0,0) &= rs. \end{aligned} \tag{23}$$

The coefficient d does not appear in the first derivatives because the term containing d carries the factor $\psi(0) - \psi(0) = 0$. The Jacobian of the map at E_0 is

$$\begin{aligned} A &= DF(E_0) \\ &= \begin{pmatrix} 1 & h & 0 \\ -as(1-r) & 1-\mu & -asr \\ 1 & 0 & 0 \end{pmatrix}. \end{aligned} \tag{24}$$

The characteristic polynomial of the Jacobian (24) is

$$P(\lambda) = \lambda^3 + b_1\lambda^2 + b_2\lambda + b_3, \tag{25}$$

with $b_1 = \mu - 2$, $b_2 = 1 - \mu + q(1-r)$, and $b_3 = qr$. Applying the Jury criterion, [13], to (25) yields the conditions $J_i(q) > 0$, $i = 1, \ldots, 4$, where

$$\begin{aligned} J_1(q) &= q, \\ J_2(q) &= 4 - 2\mu + q(1-2r), \\ J_3(q) &= \mu - q[1 + (1-\mu)r] - q^2r^2, \\ J_4(q) &= 1 - qr. \end{aligned} \tag{26}$$

The condition $J_1(q) > 0$ is satisfied for $q > 0$. For $0 < r \le 1/2$, $J_2(q) > 0$ for every $q > 0$, whereas for $r > 1/2$ it is equivalent to $q < q_F$. Moreover,

$$J_3'(q) = -[1 + (1-\mu)r] - 2qr^2 < 0, \tag{27}$$

because $1 + (1-\mu)r > 1 - r > 0$. Because $J_3(0) = \mu > 0$ and $J_3(q) \to -\infty$ as $q \to \infty$, the equation $J_3(q) = 0$ has exactly one positive root, namely q_{NS} in (20). Thus, $J_3(q) > 0$ is equivalent to $q < q_{\mathrm{NS}}$. Finally, $J_4(q) > 0$ is equivalent to $q < q_D$.

Evaluating J_3 at $q_D = 1/r$ gives

$$J_3(q_D) = 2\mu - 2 - \frac{1}{r} = 2[\mu - \mu_c(r)]. \tag{28}$$

Because J_3 is strictly decreasing and $J_3(q_{\mathrm{NS}}) = 0$, one obtains $q_{\mathrm{NS}} < q_D$ for $\mu < \mu_c(r)$, $q_{\mathrm{NS}} = q_D$ for $\mu = \mu_c(r)$, and $q_{\mathrm{NS}} > q_D$ for $\mu > \mu_c(r)$.

For $1/2 < r < 1$,

$$q_F - q_D = \frac{2[\mu_c(r) - \mu]}{2r - 1}. \tag{29}$$

Hence $q_F > q_D$ for $\mu < \mu_c(r)$, $q_F = q_D$ for $\mu = \mu_c(r)$, and $q_F < q_D$ for $\mu > \mu_c(r)$. Comparing q_{NS} with q_D and q_F with q_D gives $q_{\mathrm{NS}} < q_D < q_F$ for $\mu < \mu_c(r)$ and $q_F < q_D < q_{\mathrm{NS}}$ for $\mu > \mu_c(r)$. If $0 < r \le 1/2$, then $\mu_c(r) \ge 2$; since $0 < \mu < 2$, it follows that $q_{\mathrm{NS}} < q_D$, and $J_2(q) = 0$ has no positive root. The intersection of $J_i(q) > 0$, $i = 1, \ldots, 4$, gives (21). □

At $q = 0$, the characteristic polynomial has the factor $\lambda - 1$, so E_0 is not Schur-stable. For $r > 1/2$ and $\mu = \mu_c(r)$, the three candidate boundaries coincide: $q_{\mathrm{NS}} = q_F = q_D = 1/r$. The identity $P(-1) = 2\mu - 4 + q(2r - 1)$ shows that the boundary q_F is associated with multiplier $\lambda = -1$.

Because $q = has$, the boundary in the map parameter a is $a_c = q_c/(hs)$; in particular, $a_{\mathrm{NS}} = q_{\mathrm{NS}}/(hs)$ and $a_F = q_F/(hs)$. The parameter $\mu = hT(\gamma_v + \gamma_\Delta)$ measures the strength of the speed adjustment over one update interval, whereas r is the reaction-delay fraction at the uniform-following equilibrium. The threshold $\mu_c(r)$ separates the two mechanisms of stability loss. For $\mu < \mu_c(r)$, the critical mode is oscillating. For $\mu > \mu_c(r)$, the multiplier $\lambda = -1$ produces a sign reversal of the perturbation from one update to the next update.

3.2 Spectral Conditions at the Neimark–Sacker Boundary

In the region $\mu < \mu_c(r)$, the stability boundary is q_{NS} in Eq. (20). Set $a_{\mathrm{NS}} = q_{\mathrm{NS}}/(hs)$. Proposition 3.2 provides the spectral conditions for the critical multiplier pair at $a = a_{\mathrm{NS}}$.

Proposition 3.2. *For $0 < r < 1$, $0 < \mu < \min\{2, \mu_c(r)\}$, and $h, s > 0$, at $a = a_{\mathrm{NS}}$ there exists a simple multiplier pair $e^{\pm i\omega}$, $0 < \omega < \pi/2$, together with a third multiplier of modulus less than one. The critical pair is nonresonant through order four and crosses the unit circle transversely outward as a increases.*

Proof. The identity $J_3(q_{\mathrm{NS}}) = 0$ in (26) gives

$$\mu = q_{\mathrm{NS}}[1 + (1 - \mu)r] + q_{\mathrm{NS}}^2 r^2. \tag{30}$$

Substituting $J_3(q_{\mathrm{NS}}) = 0$ into the coefficient b_2 in (25) gives

$$\begin{aligned} b_2 &= 1 - q_{\mathrm{NS}}[1 + (1 - \mu)r] \\ &\quad - q_{\mathrm{NS}}^2 r^2 + q_{\mathrm{NS}}(1 - r) \\ &= 1 - q_{\mathrm{NS}} r(2 - \mu + q_{\mathrm{NS}} r). \end{aligned} \tag{31}$$

Matching coefficients in (25) then yields the factorization

$$\begin{aligned} P(\lambda) &= (\lambda + q_{\mathrm{NS}} r) \\ &\quad \times \left[\lambda^2 - (2 - \mu + q_{\mathrm{NS}} r)\lambda + 1\right]. \end{aligned} \tag{32}$$

The real multiplier is $\lambda_3 = -q_{\mathrm{NS}} r$. From $\mu < \mu_c(r)$ and the boundary comparison in the proof of Proposition 3.1, $q_{\mathrm{NS}} < q_D = 1/r$ hence, $|\lambda_3| < 1$.

Because J_3 is strictly decreasing and $J_3(\mu/r) = -\mu/r < 0$, we have $q_{\mathrm{NS}} r < \mu$. Together with $0 < \mu < 2$, this inequality gives $0 < 2 - \mu + q_{\mathrm{NS}} r < 2$. The two roots of the quadratic factor in (32) are therefore

$$\begin{aligned} \lambda_{1,2} &= e^{\pm i\omega}, \qquad 0 < \omega < \frac{\pi}{2}, \\ \cos\omega &= \frac{2 - \mu + q_{\mathrm{NS}} r}{2}. \end{aligned} \tag{33}$$

The two roots are non-real and distinct, whereas λ_3 is real; therefore, all three multipliers are simple. For $k = 1, 2, 3, 4$, one has $0 < k\omega < 2\pi$, which ensures $e^{ik\omega} \neq 1$.

For transversality, continue the complex pair as $\lambda(q), \overline{\lambda(q)}$ near q_{NS} and denote the real multiplier by $\gamma(q)$. Set $u(q) = \mathrm{Re}\,\lambda(q)$ and $m(q) = |\lambda(q)|^2$. Vieta's formulas applied to (25) give

$$\begin{aligned} 2u + \gamma &= 2 - \mu, \\ m + 2u\gamma &= 1 - \mu + q(1 - r), \\ m\gamma &= -qr. \end{aligned} \tag{34}$$

At $q = q_{\mathrm{NS}}$, $m = 1$, $\gamma = -q_{\mathrm{NS}} r$, and $2u = 2 - \mu + q_{\mathrm{NS}} r$. A prime denotes differentiation with respect to q. Differentiating the three Vieta identities in (34) gives

$$\begin{aligned} 2u' + \gamma' &= 0, \\ m' + 2\gamma u' + 2u\gamma' &= 1 - r, \\ \gamma m' + m\gamma' &= -r. \end{aligned} \tag{35}$$

From $2u' + \gamma' = 0$, $u' = -\gamma'/2$. Since $m = 1$ at $q = q_{\mathrm{NS}}$, the remaining two identities reduce to

$$\begin{aligned} m' + (2u - \gamma)\gamma' &= 1 - r, \\ \gamma m' + \gamma' &= -r. \end{aligned} \tag{36}$$

From $\gamma m' + \gamma' = -r$, one obtains $\gamma' = -r - \gamma m'$. Substitution into $m' + (2u - \gamma)\gamma' = 1 - r$ gives

$$m'[1 - \gamma(2u - \gamma)] = 1 - r + r(2u - \gamma). \tag{37}$$

At $q = q_{\mathrm{NS}}$, $\gamma = -q_{\mathrm{NS}} r$ and $2u - \gamma = 2 - \mu + 2q_{\mathrm{NS}} r$. Therefore,

$$\left.\frac{dm}{dq}\right|_{q_{\mathrm{NS}}} = \frac{1 + r - \mu r + 2q_{\mathrm{NS}} r^2}{1 + q_{\mathrm{NS}} r(2 - \mu) + 2q_{\mathrm{NS}}^2 r^2}. \tag{38}$$

The numerator is positive because $1 + r - \mu r > 1 - r > 0$, and the denominator is positive because $2 - \mu > 0$. Since $m = |\lambda|^2$, $m' = 2|\lambda|\, d|\lambda|/dq$. At $q = q_{\mathrm{NS}}$, $|\lambda| = 1$, so

$$\left.\frac{d|\lambda|}{dq}\right|_{q_{\mathrm{NS}}} = \frac{1}{2}\left.\frac{dm}{dq}\right|_{q_{\mathrm{NS}}} > 0. \tag{39}$$

Because $q = has$, $dq/da = hs$. Hence

$$\left.\frac{\partial|\lambda|}{\partial a}\right|_{a_{\mathrm{NS}}} = \frac{hs}{2}\frac{1+r-\mu r+2q_{\mathrm{NS}}r^2}{1+q_{\mathrm{NS}}r(2-\mu)+2q_{\mathrm{NS}}^2r^2} > 0. \tag{40}$$

□

Define

$$\chi_a = \left.\frac{\partial|\lambda|}{\partial a}\right|_{a_{\mathrm{NS}}} > 0. \tag{41}$$

Since $|\lambda(a_{\mathrm{NS}})| = 1$, the local expansion in a is

$$|\lambda(a)| = 1 + \chi_a(a - a_{\mathrm{NS}}) + o(|a - a_{\mathrm{NS}}|). \tag{42}$$

The positivity of χ_a in (40) yields $|\lambda(a)| < 1$ for $a < a_{\mathrm{NS}}$ sufficiently close to the boundary and $|\lambda(a)| > 1$ for $a > a_{\mathrm{NS}}$ sufficiently close to it. Thus, the critical pair crosses the unit circle transversely outward.

The linear analysis determines the location and direction of critical crossing. Determining whether the Neimark–Sacker bifurcation is supercritical or subcritical requires the first Lyapunov coefficient, which is computed in Section 4.

4 Neimark–Sacker Criticality and Chenciner Degeneracy

The Jacobian at $E_0 = (0, 0, 0)$ does not contain $d = \rho'(0)$; therefore, d can affect the transition only through nonlinear terms. All normal-form coefficients are evaluated at $a = a_{\mathrm{NS}}$, where $\lambda, \bar{\lambda}$ form the simple unit-modulus pair from Proposition 3.2 and the third multiplier remains inside the unit disk. The cubic reduction requires $\lambda^k \neq 1$ for $k = 1, \ldots, 4$; the fifth-order reduction uses the corresponding non-resonance condition through $k = 6$.

4.1 First Lyapunov Coefficient

Assume that the response functions have the local expansions

$$\begin{aligned}\psi(x) &= sx + \frac{c_3}{6}x^3 + O(x^5),\\ \rho(x) &= r + dx + O(x^3).\end{aligned} \tag{43}$$

where $s = \psi'(0) > 0$, $c_3 = \psi'''(0)$, and $\rho''(0) = 0$. The coefficients s, c_3, r are held fixed, whereas d is varied. Write the mixed response as

$$\Phi(x, z) = (1 - \rho(x))\psi(x) + \rho(x)\psi(z). \tag{44}$$

Substitution of (43) gives

$$\begin{aligned}\Phi(x,z) = {}& [1 - r - dx + O(x^3)]\\ &\times [sx + \tfrac{1}{6}c_3x^3 + O(x^5)]\\ &+ [r + dx + O(x^3)]\\ &\times [sz + \tfrac{1}{6}c_3z^3 + O(z^5)].\end{aligned} \tag{45}$$

Collecting monomials through degree three gives

$$\begin{aligned}\Phi(x,z) = {}& s[(1-r)x + rz] + sd(xz - x^2)\\ &+ \frac{c_3}{6}[(1-r)x^3 + rz^3]\\ &+ O(\|(x,z)\|^4).\end{aligned} \tag{46}$$

The terms containing d are all quadratic. The cubic contribution in (46) is independent of d.

For $X = (x, y, z)^\top$, write the map expansion as

$$\begin{aligned}F(X) = {}& AX + \frac{1}{2}B(X,X) + \frac{1}{6}C(X,X,X)\\ &+ O(\|X\|^4), \qquad A = D_XF(E_0).\end{aligned} \tag{47}$$

In (47), $B := D_X^2F(E_0)$ and $C := D_X^3F(E_0)$ are symmetric multilinear forms with codomains $\mathbb{R}^3$. Their domains are $(\mathbb{R}^3)^2$ and $(\mathbb{R}^3)^3$, respectively. The evaluation of complex eigenvectors uses unique complex multilinear extensions. Only the second component of F contains nonlinear terms through $-a\Phi(x, z)$. Differentiating (46) therefore gives, for $U = (u_1, u_2, u_3)^\top$ and analogously V, W,

$$B(U,V) = a\,s\,d\begin{pmatrix}0\\ 2u_1v_1 - (u_1v_3 + u_3v_1)\\ 0\end{pmatrix}, \tag{48}$$

$$C(U,V,W) = -ac_3\begin{pmatrix}0\\ (1-r)u_1v_1w_1 + ru_3v_3w_3\\ 0\end{pmatrix}. \tag{49}$$

From (48)–(49), we write $B = dB_1$ and $C = C_0$; the forms B_1 and C_0 are independent of d.

At the boundary $a = a_{\mathrm{NS}}$, choose the critical multiplier λ with $\operatorname{Im}\lambda > 0$. The right eigenvector $\mathbf{v}$ and adjoint eigenvector $\mathbf{p}$ satisfy

$$A\mathbf{v} = \lambda\mathbf{v}, \quad A^\top\mathbf{p} = \bar{\lambda}\mathbf{p}, \quad \langle\mathbf{p}, \mathbf{v}\rangle = 1. \tag{50}$$

where $\langle\mathbf{p}, U\rangle = \bar{\mathbf{p}}^\top U$. The symbol $\mathbf{v}$ is reserved for the eigenvector; $q = has$ remains a scalar gain parameter. From the first and third rows of $A\mathbf{v} = \lambda\mathbf{v}$, $v_2 = (\lambda - 1)v_1/h$ and $v_3 = v_1/\lambda$. The adjoint equation gives $p_1 = (\bar{\lambda} - 1 + \mu)p_2/h$ and $p_3 = -asrp_2/\bar{\lambda}$. We therefore use

$$\begin{aligned}\widetilde{\mathbf{v}} &= \begin{pmatrix}1\\ (\lambda-1)/h\\ \lambda^{-1}\end{pmatrix},\\ \widetilde{\mathbf{p}} &= \begin{pmatrix}(\bar{\lambda}-1+\mu)/h\\ 1\\ -asr/\bar{\lambda}\end{pmatrix}.\end{aligned} \tag{51}$$

The unused components of the eigenvector system (50) are satisfied because $P(\lambda) = 0$. With $\widetilde{\mathbf{v}}$ and $\widetilde{\mathbf{p}}$ from (51), set

$$\mathbf{v} = \frac{\widetilde{\mathbf{v}}}{\|\widetilde{\mathbf{v}}\|_2}, \qquad \mathbf{p} = \frac{\widetilde{\mathbf{p}}}{\langle\widetilde{\mathbf{p}}, \mathbf{v}\rangle}, \tag{52}$$

which gives $\|\mathbf{v}\|_2 = 1$, $v_1 > 0$, and $\langle\mathbf{p}, \mathbf{v}\rangle = 1$. The denominator in the adjoint normalization is nonzero

because λ is simple. Normalization (52) is used throughout the normal-form coefficient calculations. Because A is independent of d, both eigenvectors can be chosen independently of d along the boundary $a = a_{\mathrm{NS}}$. The complex center coordinate is chosen as $w = \langle \mathbf{p}, X \rangle$, so the linear part of the center manifold parameterization is $X = \mathbf{v}w + \bar{\mathbf{v}}\bar{w} + O(|w|^2)$.

After the quadratic terms in the reduced map are removed, the center-manifold expansion through second order is written as

$$\begin{aligned}\mathcal{H}(w,\bar{w}) = \mathbf{v}w + \bar{\mathbf{v}}\bar{w} + \tfrac{1}{2}h_{20}w^2 \\ + h_{11}w\bar{w} + \tfrac{1}{2}\bar{h}_{20}\bar{w}^2 + O(|w|^3).\end{aligned} \tag{53}$$

Matching the coefficients of w^2 and $w\bar{w}$ in $F(\mathcal{H}) = \mathcal{H}(G, \bar{G})$ gives

$$\begin{aligned}(\lambda^2 I - A)h_{20} &= B(\mathbf{v}, \mathbf{v}), \\ (I - A)h_{11} &= B(\mathbf{v}, \bar{\mathbf{v}}).\end{aligned} \tag{54}$$

The spectral conditions ensure that both matrices in (54) are invertible. Their coefficient forms can be explicitly obtained from the structure of A. For $\zeta \neq 0$ and $P(\zeta) \neq 0$, let $(\zeta I - A)U = (0, b, 0)^\top$. The first and third rows give $u_2 = (\zeta - 1)u_1/h$ and $u_3 = u_1/\zeta$. Substitution into the second row yields

$$\begin{aligned}\Big[as(1-r) + \frac{(\zeta - 1 + \mu)(\zeta - 1)}{h} \\ + \frac{asr}{\zeta}\Big]u_1 = b.\end{aligned} \tag{55}$$

The bracketed expression equals $P(\zeta)/(h\zeta)$, hence

$$(\zeta I - A)^{-1}\begin{pmatrix}0\\ b\\ 0\end{pmatrix} = \frac{b}{P(\zeta)}\begin{pmatrix}h\zeta\\ \zeta(\zeta-1)\\ h\end{pmatrix}. \tag{56}$$

Next, the relations $v_3 = v_1/\lambda$ and $|\lambda| = 1$ in (48) give

$$\begin{aligned}B(\mathbf{v}, \mathbf{v}) &= 2a\, s\, d\, v_1^2(1 - \lambda^{-1})\begin{pmatrix}0\\1\\0\end{pmatrix}, \\ B(\mathbf{v}, \bar{\mathbf{v}}) &= 2a\, s\, d\, |v_1|^2(1 - \operatorname{Re}\lambda)\begin{pmatrix}0\\1\\0\end{pmatrix}.\end{aligned} \tag{57}$$

Using (56) at $\zeta = \lambda^2$ and $\zeta = 1$, with $P(1) = has$, gives

$$\begin{aligned}h_{20} &= \frac{2a\, s\, d\, v_1^2(1 - \lambda^{-1})}{P(\lambda^2)}\begin{pmatrix}h\lambda^2\\ \lambda^2(\lambda^2 - 1)\\ h\end{pmatrix}, \\ h_{11} &= 2d|v_1|^2(1 - \operatorname{Re}\lambda)\begin{pmatrix}1\\0\\1\end{pmatrix}.\end{aligned} \tag{58}$$

The formulas for h_{20} and h_{11} in (58) are linear in d. Therefore,

$$h_{20} = dh_{20}^{(1)}, \qquad h_{11} = dh_{11}^{(1)}, \tag{59}$$

where $h_{20}^{(1)}$ and $h_{11}^{(1)}$ are obtained from (58) by replacing the factor d with 1.

Use the convention $G(w, \bar{w}) = \lambda w + g_{21}w^2\bar{w} + O(|w|^4)$ and write the coefficient of $w^2\bar{w}$ in the center manifold as $h_{21}/2$. Matching the monomial $w^2\bar{w}$ in the invariance equation gives

$$\begin{aligned}(\lambda I - A)h_{21} = C_0(\mathbf{v}, \mathbf{v}, \bar{\mathbf{v}}) + B(\bar{\mathbf{v}}, h_{20}) \\ + 2B(\mathbf{v}, h_{11}) - 2g_{21}\mathbf{v}.\end{aligned} \tag{60}$$

Since $\bar{\mathbf{p}}^\top(\lambda I - A) = 0$, projection of (60) onto $\mathbf{p}$ determines the resonant coefficient

$$\begin{aligned}g_{21} = \frac{1}{2}\big\langle \mathbf{p}, C_0(\mathbf{v}, \mathbf{v}, \bar{\mathbf{v}}) + B(\bar{\mathbf{v}}, h_{20}) \\ + 2B(\mathbf{v}, h_{11})\big\rangle, \\ \ell_1 = \operatorname{Re}(\bar{\lambda} g_{21}).\end{aligned} \tag{61}$$

After g_{21} is determined, h_{21} is obtained from (60) under the normalization $\langle \mathbf{p}, h_{21} \rangle = 0$. This condition removes the freedom to add a multiple of $\mathbf{v}$ to the solution of the singular homological equation.

Proposition 4.1. *Under* (43) *and the spectral conditions of Proposition 3.2, the first Lyapunov coefficient at $a = a_{\mathrm{NS}}$ satisfies*

$$\ell_1(d) = c_0 + c_2 d^2, \tag{62}$$

where c_0 and c_2 are independent of d.

Proof. Substituting $B = dB_1$ and (59) into (61) gives

$$\begin{aligned}g_{21}(d) &= g_{21}^{(0)} + d^2 g_{21}^{(2)}, \\ g_{21}^{(0)} &= \tfrac{1}{2}\langle \mathbf{p}, C_0(\mathbf{v}, \mathbf{v}, \bar{\mathbf{v}})\rangle, \\ g_{21}^{(2)} &= \tfrac{1}{2}\langle \mathbf{p}, B_1(\bar{\mathbf{v}}, h_{20}^{(1)}) + 2B_1(\mathbf{v}, h_{11}^{(1)})\rangle.\end{aligned} \tag{63}$$

Each quadratic contribution contains two factors of d, one from B and the other from the center manifold coefficient. Taking the real part after multiplication by $\bar{\lambda}$ gives $c_j = \operatorname{Re}(\bar{\lambda} g_{21}^{(j)})$ for $j = 0, 2$, thus proving (62). □

Let $\chi_a = \partial_a |\lambda(a)|_{a=a_{\mathrm{NS}}}$, which is positive by (40). The sign $\ell_1 < 0$ in (61) indicates a supercritical bifurcation with an attracting invariant curve for $a > a_{\mathrm{NS}}$, whereas $\ell_1 > 0$ indicates a subcritical bifurcation with an unstable invariant curve for $a < a_{\mathrm{NS}}$. In the model, r in (19) determines where uniform following loses linear stability through (20), whereas d determines the criticality through (62). Therefore, two systems with the same a_{NS} can undergo different nonlinear transitions.

4.2 Cubic Degeneracy and Fold Prediction

If $c_0 c_2 < 0$, the positive root of (62) is

$$d^* = \sqrt{-c_0/c_2}, \qquad \ell_1'(d^*) = 2c_2 d^* \neq 0. \tag{64}$$

At $d = d^*$ from (64), the cubic radial term vanishes. The fifth-order coefficient requires derivatives that are not specified in (43). It is evaluated for the benchmark family

$$\begin{aligned}\psi(x) &= \tanh x, \\ \rho_d(x) &= r + \delta_0 \tanh(dx/\delta_0), \\ (h, \mu, r, \delta_0) &= (1, 0.8, 0.6, 0.3).\end{aligned} \tag{65}$$

The benchmark family (65) satisfies $0.3 < \rho_d(x) < 0.9$ for all x.

The expansion $\tanh x = x - x^3/3 + 2x^5/15 + O(x^7)$ gives

$$\rho_d(x) = r + dx - \frac{d^3}{3\delta_0^2}x^3 + O(x^5). \tag{66}$$

Because $\rho_d(x)$ multiplies $\psi(z) - \psi(x)$, which has no constant term, the fifth-degree term in ρ_d first contributes at degree six in Φ. Write $\Phi = \sum_{m=1}^{5} \Phi_m + O(\|(x,z)\|^6)$, where Φ_m is homogeneous of degree m. Multiplying the two expansions gives

$$\begin{aligned}
\Phi_1 &= (1-r)x + rz,\\
\Phi_2 &= d(xz - x^2),\\
\Phi_3 &= -\tfrac{1}{3}[(1-r)x^3 + rz^3],\\
\Phi_4 &= -\tfrac{d}{3}x(z^3 - x^3) - \frac{d^3}{3\delta_0^2}x^3(z-x),\\
\Phi_5 &= \tfrac{2}{15}[(1-r)x^5 + rz^5].
\end{aligned} \tag{67}$$

Thus the fifth-order Taylor polynomial of the map is

$$F_5(X) = AX - a\begin{pmatrix} 0 \\ \Phi_2 + \Phi_3 + \Phi_4 + \Phi_5 \\ 0 \end{pmatrix}. \tag{68}$$

The term Φ_4 in (67) indicates how the third derivative of the delay function enters the fifth-order calculation through center-manifold matching.

The homological calculation follows the normal form construction for maps in [14]. Use the factorial convention

$$\begin{aligned}
\mathcal{H}(w,\bar w) &= \mathbf{v}w + \bar{\mathbf{v}}\bar w + \sum_{2\le j+k\le 5} \frac{h_{jk}}{j!k!} w^j \bar w^k,\\
G(w,\bar w) &= \lambda w + g_{21}w^2\bar w\\
&\quad + g_{32}w^3\bar w^2 + O(|w|^6).
\end{aligned} \tag{69}$$

In (69), $h_{kj} = \bar h_{jk}$, whereas g_{21} and g_{32} multiply monomials without factorial factors.

Let $\mathcal{H}_{<m}$ and $G_{<m}$ contain terms of degree less than m. If $[Q]_{jk}$ denotes the coefficient of $w^j\bar w^k$, the residual determined by lower orders is

$$\begin{aligned}
R_{jk}^{(m)} = j!k!\Big[&F_5(\mathcal{H}_{<m})\\
&- \mathcal{H}_{<m}(G_{<m}, \bar G_{<m})\Big]_{jk},\\
&j + k = m.
\end{aligned} \tag{70}$$

Define the degree-five truncated invariance defect by

$$\mathcal{E}_5 = \big[F_5(\mathcal{H}) - \mathcal{H}(G,\bar G)\big]_{\le 5}, \tag{71}$$

and

$$\varepsilon_5 := \max_{2\le j+k\le 5} \big\|[\mathcal{E}_5]_{jk}\big\|_2. \tag{72}$$

The norm in (72) is the Euclidean norm on $\mathbb{C}^3$. For nonresonant monomials, solve

$$(\lambda^j\bar\lambda^k I - A)h_{jk} = R_{jk}^{(m)}. \tag{73}$$

For the resonant pairs $(j,k) = (2,1)$ and $(3,2)$, the condition $\langle \mathbf{p}, h_{jk}\rangle = 0$ completes the bordered system

$$\begin{pmatrix} \lambda I - A & \mathbf{v} \\ \bar{\mathbf{p}}^{\top} & 0 \end{pmatrix}\begin{pmatrix} h_{jk} \\ j!k!g_{jk} \end{pmatrix} = \begin{pmatrix} R_{jk}^{(m)} \\ 0 \end{pmatrix}. \tag{74}$$

Multiplying the first row by $\bar{\mathbf{p}}^{\top}$ gives

$$g_{21} = \tfrac{1}{2}\langle \mathbf{p}, R_{21}^{(3)}\rangle, \qquad g_{32} = \tfrac{1}{12}\langle \mathbf{p}, R_{32}^{(5)}\rangle. \tag{75}$$

The system in (74) also determines h_{21}, which enters the degree-four and degree-five residuals through (70).

Set $\gamma = \bar\lambda g_{21}$ and $\zeta = \bar\lambda g_{32}$. With $R = |w|$, the terms retained in (69) give

$$\begin{aligned}
|1 + \gamma R^2 + \zeta R^4|^2 = 1 &+ 2\,\mathrm{Re}(\gamma)R^2\\
&+ \big(|\gamma|^2 + 2\,\mathrm{Re}(\zeta)\big)R^4\\
&+ O(R^6).
\end{aligned} \tag{76}$$

Expanding the square root of (76) gives the R^4 coefficient $\mathrm{Re}(\zeta) + \frac{1}{2}[\mathrm{Im}(\gamma)]^2$. At $d = d^*$, the fifth-order radial coefficient is therefore

$$\beta_2(d^*) = \mathrm{Re}(\bar\lambda g_{32}) + \frac{1}{2}[\mathrm{Im}(\bar\lambda g_{21})]^2. \tag{77}$$

For the benchmark (65), evaluation of (61) with the normalization (50) gives

$$\begin{aligned}
a_{\mathrm{NS}} &\approx 0.598968826,\\
\ell_1(d) &\approx -0.11266336 + 0.028056622\,d^2,\\
d^* &\approx 2.003889,\\
\ell_1'(d^*) &\approx 0.112445.
\end{aligned} \tag{78}$$

At $d = d^*$ in (78), $\lambda \approx 0.779691 + 0.626165\,i$ and the third multiplier is approximately -0.359381. Equations (70)–(74), followed by (77), yield $\beta_2(d^*) \approx -4.45553$.

For the two-parameter unfolding, set $\nu(a) = |\lambda(a)| - 1$ and let $L(a,d)$ denote a smooth continuation of the cubic radial coefficient, with $L(a_{\mathrm{NS}}, d) = \ell_1(d)$. Because ν is independent of d,

$$\begin{aligned}
\det D_{(a,d)}(\nu, L)\big|_{(a_{\mathrm{NS}}, d^*)} &= \chi_a \ell_1'(d^*)\\
&\approx 0.051620 \neq 0,\\
\chi_a &\approx 0.459069.
\end{aligned} \tag{79}$$

For the benchmark in (65), Proposition 3.2 supplies a simple critical pair. The pair is nonresonant through order six, (78) gives $\ell_1(d^*) = 0$, (79) has a nonzero determinant, and (77) gives $\beta_2(d^*) \neq 0$. These conditions numerically identify the benchmark point as the Chenciner point.

The leading terms of the radial equation near $(a,d) = (a_{\mathrm{NS}}, d^*)$ are

$$\begin{aligned}
R_{n+1} - R_n = R_n[\nu + \ell_1(d)R_n^2 + \beta_2(d^*)R_n^4]\\
+ \text{higher-order terms.}
\end{aligned} \tag{80}$$

The full cubic coefficient differs from $\ell_1(d)$ by $O(|a - a_{\mathrm{NS}}|)$, whereas the quintic coefficient differs from $\beta_2(d^*)$ by $O(|a - a_{\mathrm{NS}}| + |d - d^*|)$. These higher-order corrections do not alter the leading-order fold predictor, (83). For a nonzero radius, set $S = R^2 > 0$.

A fold of the truncated radial equation satisfies

$$\begin{aligned} \nu + \ell_1(d)S + \beta_2(d^*)S^2 = 0, \\ \ell_1(d) + 2\beta_2(d^*)S = 0. \end{aligned} \tag{81}$$

Eliminating S from (81) gives

$$S_{\text{fold}} = -\frac{\ell_1(d)}{2\beta_2(d^*)} > 0, \qquad \nu_{\text{fold}} = \frac{\ell_1(d)^2}{4\beta_2(d^*)}. \tag{82}$$

Substituting $\nu = \chi_a(a - a_{\text{NS}}) + O((a - a_{\text{NS}})^2)$ into (82) yields the local prediction in the original parameter,

$$\begin{aligned} a_{\text{fold}}(d) = a_{\text{NS}} + \frac{\ell_1(d)^2}{4\chi_a\beta_2(d^*)} + o((d - d^*)^2), \\ d \downarrow d^*. \end{aligned} \tag{83}$$

For $d > d^*$, (78) gives $\ell_1(d) > 0$, while (77) gives $\beta_2(d^*) < 0$. Hence, (83) places $a_{\text{fold}}(d)$ below a_{NS} by an amount of order $(d - d^*)^2$. Through (19), d is the local slope of the reaction-delay fraction with respect to the normalized headway. In the benchmark, a slope beyond d^* creates a parameter interval $a_{\text{fold}}(d) < a < a_{\text{NS}}$ in which E_0 is still Schur stable, but a finite-amplitude invariant curve is also present. Section 5 locates this interval by continuation and tests which attractor is reached from different initial headway perturbations.

5 Continuation and Coexistence

Fix $(h, \mu, r, \delta_0) = (1, 0.8, 0.6, 0.3)$ as in (65). The choices $d = 0 < d^*$ and $d = 3 > d^*$ give opposite signs of ℓ_1 in (78), while a_{NS} remains unchanged because d does not enter the Jacobian. Because a_{NS} is identical in the two cases, the continuation isolates the effect of the local headway sensitivity of the reaction delay. The fold scan uses $2.02 \le d \le 3$.

Each oscillatory state is represented by a periodic parameterization K satisfying

$$\begin{aligned} F_{a,d}(K(\theta)) = K(\theta + \omega), \\ K(\theta + 2\pi) = K(\theta). \end{aligned} \tag{84}$$

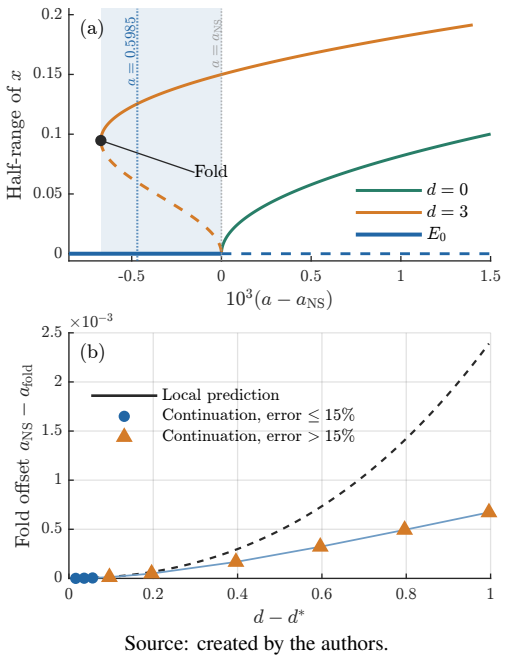
A 95-point Fourier collocation discretizes (84). The first cosine coefficient of K_x parameterizes the branch, and its first sine coefficient is set to zero to fix the phase. The critical eigenvector provides an initial curve. In subsequent steps, the previous solution supplies the starting point, while a, ω, and the Fourier coefficients of K are solved together; this continuation passes through the fold. Figure 2(a) shows half the range of K_x. Proposition 3.1 supplies the stability of E_0 on the same $a$axis.

At $d = 0$, the attracting invariant curve shrinks to E_0 as $a \to a_{\text{NS}}^+$. Thus, near the threshold, a follower that started close to uniform following developed only small-amplitude oscillations after E_0 lost Schur stability. For $d = 3$, continuation follows the attracting invariant curve into $a < a_{\text{NS}}$ until it meets the saddle branch at $a_{\text{fold}} \approx 0.598297$. For $0.598297 \lesssim a < a_{\text{NS}}$, E_0 remains Schur stable, and a stable finite-amplitude invariant curve is also present. Since $d = \rho'(0)$ does not enter the Jacobian, this coexistence interval comes from the nonlinear dependence of the reaction delay on headway, not from a displacement of a_{NS}.

At $(a, d) = (0.5985, 3)$, the two transverse exponents of the outer curve are negative, whereas the inner curve has one positive and one negative transverse exponent. Therefore, the outer curve is attractive, and the inner curve is saddle-shaped. Their meeting point is identified by the local minimum of a along the continued branch. Increasing the collocation size from 63 to 95 points changes this minimum by less than 2×10^{-15} at $d = 2.02, 2.2, 3$; the largest invariance residual over 1021 phases remains below 7×10^{-14}.

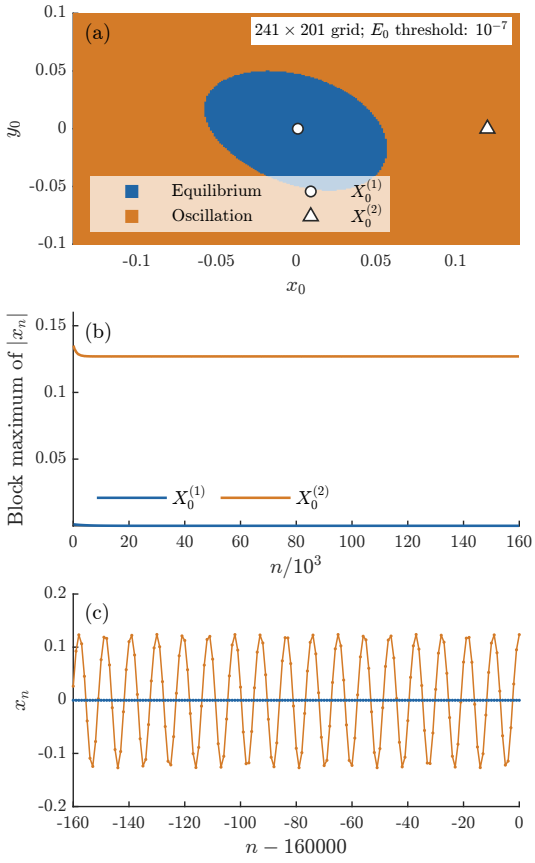
At $d = d^*$, the degree-five coefficient equations have the largest componentwise residual of approximately 2.1×10^{-15} in double precision, and (72) gives $\varepsilon_5 \approx 8.6 \times 10^{-15}$. Solving the same equations at 50, 70, and 90 digits leaves $\beta_2(d^*)$ unchanged to 12 decimal places, while ε_5 falls from approximately 8×10^{-50} to 7×10^{-90}. The noncritical multiplier has a modulus of approximately 0.359, so it is separated from the unit circle at the benchmark point.

To compare the local formula with the continued fold, set $a_{\text{fold}}^{\text{pred}}$ equal to the leading term of (83), and let $a_{\text{fold}}^{\text{cont}}$ be the continuation value. Normalize their



Source: created by the authors.

Figure 2: Continuation for the benchmark (65). Panel (a) shows the invariant-curve half-range for $d = 0$ and $d = 3$; the solid and dashed segments represent the attracting and unstable segments, respectively. For $d = 3$, the shaded interval lies between the fold and a_{NS}, and the blue line marks $a = 0.5985$. Panel (b) plots $a_{\text{NS}} - a_{\text{fold}}$ against $d - d^*$ for (83) and continuation, respectively. Circles correspond to errors at most 15%; triangles correspond to larger errors.



Source: created by the authors.

Figure 3: Coexistence at $(a, d) = (0.5985, 3)$. Panel (a) classifies the section $z_0 = x_0$ on a 241×201 grid, where the equilibrium class uses the threshold 10^{-7}. The circle marks $X_0^{(1)} = (0.001, 0, 0.001)$ and the triangle marks $X_0^{(2)} = (0.12, 0, 0.12)$. Panel (b) gives the 200-iteration block maxima of $|x_n|$, and panel (c) gives the last 160 iterates of the same two trajectories.

difference by the continued fold displacement,

$$\varepsilon_{\text{fold}} = \frac{|a_{\text{fold}}^{\text{pred}} - a_{\text{fold}}^{\text{cont}}|}{|a_{\text{NS}} - a_{\text{fold}}^{\text{cont}}|}. \tag{85}$$

Figure 2(b) shows the Chenciner value $\beta_2(d^*)$ from (77) throughout the scan. Equation (85) gives about 2.5% error at $d = 2.02$ and more than 15% from the sampled value $d = 2.10$ onward; at $d = 3$ the error is about 256%. The 15% threshold is already crossed at $d = 2.10$, so (83) is quantitatively useful only when close to the local slope d^*. Accordingly, the coexistence calculation uses the continued value of $a_{\text{fold}}(3)$ rather than the local predictor value. As $d - d^*$ increases on the subcritical side, the continued fold moves farther below a_{NS}, widening the interval of a in which the stable uniform following coexists with a finite-amplitude invariant curve. For the benchmark, $d = \rho'(0)$ which controls both the change in Neimark–Sacker criticality and the width of the coexistence window resolved by continuation.

Set $(a, d) = (0.5985, 3)$. Continuation gives $a_{\text{fold}}(3) < 0.5985$, while Proposition 3.1 gives the stability of E_0 because $0.5985 < a_{\text{NS}}$. Hence, $(a, d) = (0.5985, 3)$ lies inside the coexistence interval identified in Figure 2(a). Figure 3(a) samples the section $z_0 = x_0$ on a 241×201 grid to determine which initial headway, relative speed, and one-step history perturbations approach each attractor. The orbits were advanced in blocks of 4096 iterations, with a maximum of 163840 iterations.

The equilibrium label is assigned when $\max \|X_n\|_\infty < 10^{-7}$ within the block. For the oscillatory label, the extrema must agree with the reference orbit within 0.2% of its range, and the range must change by less than 0.1% across three consecutive blocks after at least six blocks. The reference orbit was formed after 160000 transient iterations and then sampled for 16384 iterations. A separate 64-point check yielded the same classifications.

The two marked initial conditions in Figure 3 have $y_0 = 0$ and $z_0 = x_0$, and thus differ only in the size of the headway/history displacement. The state $X_0^{(1)} = (0.001, 0, 0.001)$ returns to E_0, whereas $X_0^{(2)} = (0.12, 0, 0.12)$ approaches the oscillatory attractor and remains there through 160000 iterations. Panel (b) separates these outcomes through the block maxima of $|x_n|$, and panel (c) resolves the persistent oscillation. At $a = 0.5985 < a_{\text{NS}}$, infinitesimal perturbations still decay, but the larger headway/history displacement $X_0^{(2)}$ selects an oscillatory state. The boundary in Figure 3(a) is consistent with the stable manifold of the saddle-invariant curve. Because $x = (g - g^*)/S$, the coordinate $x_0 = 0.12$ represents a headway displacement $0.12S$ for the implication, no dimensional traffic amplitude is implied until the scale S is calibrated.

6 Conclusions

The decomposition in (19) separates the two roles of the reaction delay. The value $r = \rho(0)$ enters the Jacobian and fixes the linear threshold through the equation (20). The slope $d = \rho'(0)$ enters the quadratic terms and changes the sign of ℓ_1 through (62). For the benchmark, $d = 3$ produces a fold at $a_{\text{fold}} \approx 0.598297 < a_{\text{NS}}$. At $a = 0.5985$, the initial state $(0.001, 0, 0.001)$ returns to a uniform following, while $(0.12, 0, 0.12)$ approaches the oscillatory attractor, although E_0 remains linearly stable. In this single-follower map, the headway dependence of the reaction delay changes the response to finite perturbations without moving the linear stability boundary. Whether the same oscillation amplifies along a platoon cannot be inferred from (16); string stability, wave propagation, and physical amplitudes require a multi-vehicle extension and calibration of the dimensional scales.

References

[1] Yuki Sugiyama, Minoru Fukui, Macoto Kikuchi, Katsuya Hasebe, Akihiro Nakayama, Katsuhiro Nishinari, Shin-ichi Tadaki, and Satoshi Yukawa. Traffic jams without bottlenecks—experimental evidence for the physical mechanism of the formation of a jam. *New Journal of Physics*, 10(3):033001, 2008. doi:10.1088/1367-2630/10/3/033001.

[2] Masako Bando, Katsuya Hasebe, Akihiro Nakayama, Akira Shibata, and Yuki Sugiyama. Dynamical model of traffic congestion and numerical simulation. *Physical Review E*, 51(2):1035–1042, 1995. doi:10.1103/PhysRevE.51.1035.

[3] Rui Jiang, Qingsong Wu, and Zuojin Zhu. Full velocity difference model for a car-following theory. *Physical Review E*, 64(1):017101, 2001. doi:10.1103/PhysRevE.64.017101.

[4] Ingenuin Gasser, Gabriele Sirito, and Bodo Werner. Bifurcation analysis of a class of "Car Following" traffic models. *Physica D: Nonlinear Phenomena*, 197(3–4):222–241, 2004. doi:10.1016/j.physd.2004.07.008.

[5] Masako Bando, Katsuya Hasebe, Ken Nakanishi, and Akihiro Nakayama. Analysis of optimal velocity model with explicit delay. *Physical Review E*, 58(5):5429–5435, 1998. doi:10.1103/PhysRevE.58.5429.

[6] Gábor Orosz, Bernd Krauskopf, and R. Eddie Wilson. Bifurcations and multiple traffic jams in a car-following model with reaction-time delay. *Physica D: Nonlinear Phenomena*, 211(3–4):277–293, 2005. doi:10.1016/j.physd.2005.09.004.

[7] Gábor Orosz and Gábor Stépán. Subcritical hopf bifurcations in a car-following model with reaction-time delay. *Proceedings of the Royal Society A: Mathematical, Physical and Engineering Sciences*, 462(2073):2643–2670, 2006. doi:10.1098/rspa.2006.1660.

[8] Zhi Xin and Jian Xu. Analysis of a car-following model with driver memory effect. *International Journal of Bifurcation and Chaos*, 25(04):1550057, 2015. doi:10.1142/S0218127415500571.

[9] Kristof Martinovich, Gabor Stepan, Daniel Bachrathy, and Adam K. Kiss. Introducing state-dependent delay in the car-following model. *Nonlinear Dynamics*, 113(17):22923–22941, 2025. doi:10.1007/s11071-025-11275-0.

[10] Wen-Xing Zhu and Li-Dong Zhang. Discrete car-following model and its feedback control scheme. *Asian Journal of Control*, 22(1):182–191, 2020. doi:10.1002/asjc.1867.

[11] Tong Zhou, Dong Chen, Linjiang Zheng, Weining Liu, Yuchu He, and Zhongcheng Liu. Feedback-based control for coupled map car-following model with time delays on basis of linear discrete-time system. *Physica A: Statistical Mechanics and its Applications*, 512:174–185, 2018. doi:10.1016/j.physa.2018.08.122.

[12] Juan Francisco Padial and Alfonso Casal. Bifurcation in car-following models with time delays and driver and mechanic sensitivities. *Revista de la Real Academia de Ciencias Exactas, Físicas y Naturales. Serie A. Matemáticas*, 116(4):180, 2022. doi:10.1007/s13398-022-01307-4.

[13] Eliahu I. Jury. *Theory and Application of the Z-Transform Method*. Wiley, New York, 1964. ISBN: 978-0-471-45345-1. Google Books, Wiley 1964 edition. Accessed Date: October, 8, 2026.

[14] Yuri A. Kuznetsov and Hil G. E. Meijer. Numerical normal forms for codim 2 bifurcations of fixed points with at most two critical eigenvalues. *SIAM Journal on Scientific Computing*, 26(6):1932–1954, 2005. doi:10.1137/030601508.

Contribution of Individual Authors to the Creation of a Scientific Article (Ghostwriting Policy)

H.K.F. formulated the model, performed the analysis and computations, and drafted the manuscript. R.H.S.U. reviewed the interpretation and numerics; Y.D.S. reviewed the proofs. All authors approved the manuscript.

Sources of Funding

This research was supported under the Decree of the Head of the Institute for Research and Community Service (LPPM), Universitas Diponegoro, No. 8/UN7.A/HK/V/2026 dated May 5, 2026 and Contract Agreement No. 306-155/UN7.D2/PP/V/2026 dated May 5, 2026.

Conflict of Interest

The authors have no conflicts of interest to declare that are relevant to the content of this article.

Creative Commons Attribution License 4.0 (Attribution 4.0 International, CC BY 4.0)
This article is published under the terms of the Creative Commons Attribution License 4.0
https://creativecommons.org/licenses/by/4.0/deed.en_US

Appendix

Table 1: The table compares car-following models by time representation, delay formulation, and reported dynamical result.

Study	Time representation	Delay formulation	Main analysis or result
[5]	Continuous	Constant explicit delay	Effect of delay on congestion patterns
[6], [7]	Continuous	Constant reaction time	Periodic solutions, subcritical Hopf bifurcation, and bistability
[8]	Continuous	State-dependent delay through driver memory	Stability region and hysteresis
[12]	Continuous	Driver-reaction and mechanical delays	Stability changes, oscillatory solutions, and Hopf bifurcation
[9]	Continuous	Headway-dependent reaction time	Bistability of uniform motion and stop-and-go traffic
[10]	Discrete	Discretization with a sampling interval	Discrete stability conditions and feedback control
[11]	Discrete (coupled map)	Delay in a discrete model	Linear discrete-system analysis and feedback control

Source: created by the authors.